Fcnsic
LC03-2113

Demonstration of extreme wavefront sensing performance on the TPF high contrast imaging testbed

Joseph J. Green*, Scott A. Basinger, David Cohen, Albert F. Niessner, David C. Redding,
Stuart B. Shaklan and John T. Trauger
Jet Propulsion Laboratory, California Institute of Technology

ABSTRACT

The Terrestrial Planet Finder (TPF) high contrast imaging testbed (HCIT) facilitates the investigation into the diversity of engineering challenges presented by the goal of direct exo-planet detection. For instance, HCIT offers a high-density deformable mirror to control the optical wavefront errors, a configurable coronagraph to control the diffracted light, and translatable cameras for measuring the focal and pupil planes before and after the coronagraph. One of the principle challenges for a coronagraphic space telescope is the extreme level of wavefront control required to make the very faint planet signal reasonably detectable. A key component, the extremely accurate sensing of the wavefront aberrations, was recently shown to be achievable using a sufficiently constrained image-based approach. In this paper, we summarize the experimental performance a focus-diverse phase-retrieval method that uses symmetrically defocus point-spread function measurements that are obtained about the coronagraph occulter focal plane. Using the HCIT, we demonstrate the high level of wavefront sensing repeatability achieved with our particular choices of focus diversity, data fidelity and processing methodologies. We compare these results to traceable simulations to suggest a partitioning of the error sources that may be limiting the experimental results.

Keywords: coronagraph, wavefront sensing, phase-retrieval, focus-diversity, wavefront control

1. INTRODUCTION

Achieving and maintaining the required sub-Angstrom level of wavefront control necessary to enable planet detection is challenging to say the least. The initial deployment of a coronagraphic telescope and its subsequent cooling down will leave its optical alignments as well as the figure of its optical surfaces in poor shape for planet finding. Before the science can begin, these relatively large wavefront errors (WFE) must be reduced using the available optical degrees of freedom (i.e. using primary mirror figure actuators, secondary mirror support actuators, deformable mirrors, etc.). To correct the WFE, however, it must first be sensed accurately.

Recently, we demonstrated that the baseline wavefront sensing (WFS) method under consideration for the James Webb Space Telescope[1] was accurate to levels well below $\lambda/100$.[2] In other work, we have shown *in simulations* that this approach, the modified Gerchberg-Saxton (MGS) algorithm, can be made to achieve WFS accuracies on the order of $\lambda/10{,}000$.[3] Specifically, by collecting symmetrically defocused point-spread functions and using appropriate *model-adaptation* (see ref. [3]) to minimize the model-to-data mismatches, extremely accurate WFS may be achievable.

In this paper, we present the results of the experimental WFS performance of MGS on the Terrestrial Planet Finder (TPF) high contrast imaging testbed (HCIT). Using the MGS algorithm with its recently suggested refinements, we processed the long series of repeated WFS data collection runs in to a sequence of estimates. In the sections below, we detail the results of the experiment, documenting the extraordinary level of WFS repeatability that was achieved. We then compare these results to the repeatability of a series of WFS simulations that paralleled the experiment. These simulations also, serve to give some insight into the actual accuracy obtainable from our MGS implementation. Additionally, we compare the experimental WFS results to an estimate of the system exit-pupil that was computed using a near-field diffraction model.

*Contact information: 4800 Oak Grove Dr., M/S 306-336, Pasadena CA 91109, E-mail: Joseph.J.Green@jpl.nasa.gov

1. THE HIGH CONTRAST IMAGING TESTBED

The HCIT is a valuable resource for developing, testing and validating the key technologies needed by TPF. It currently resides in a vacuum chamber to eliminate the laboratory seeing and to stabilize the thermal environment. At the time of this experiment, a folding flat was put in place of the original DM[4] so that the testbed could be re-aligned in preparation for the imminent arrival of a new 32x32 DM. Figure 1 shows an optical drawing of the front-end optics of testbed (used during the experiment) along with ZYGO measurements of the optics over their respective full apertures.

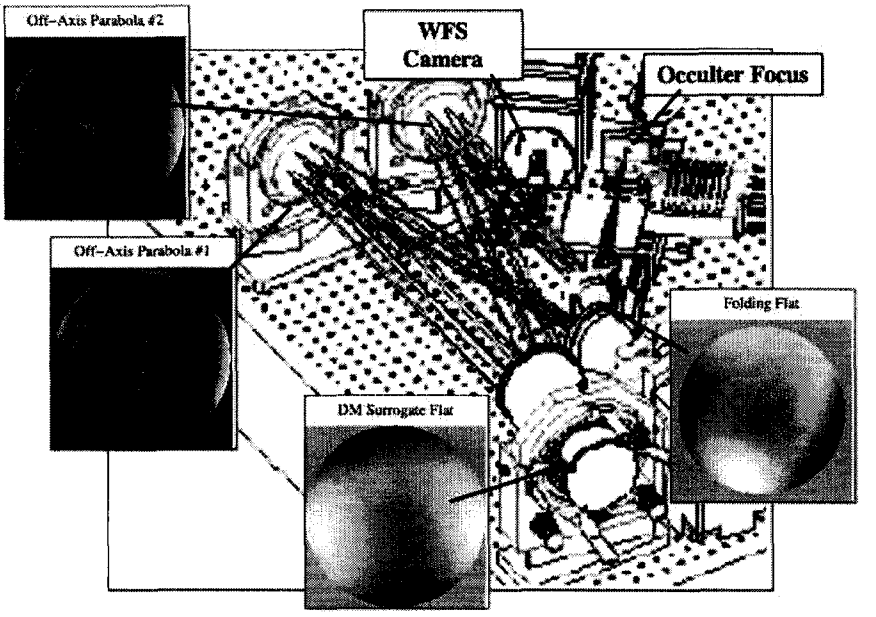

Figure 1: ZYGO measurements of front-end optics of the HCIT are shown over their clear apertures. The off-axis parabolas have a diameter of 89mm. In the experiment there is a flat mirror placed at the position of the DM along with a 30mm aperture stop (not shown) on top of it. It should be noted that the two ZYGO measurements of the flats are not shown on the same intensity scale as the off-axis parabolas measurements and have aberrations of considerably smaller magnitudes.

The diagram in Figure 1 depicts the testbed in state where the light is focused onto an occulting spot. To the left of the occulting spot there is a camera, which is used for focus-diverse WFS. Although it is hard to see in the figure both the camera and the occulting mask reside on top of a pair of crossed stages that allow us to center the camera onto the beam and take a sequence of point-spread function (PSF) measurements at and about focus.

In Figure 2, we show examples of the measurements taken during a single WFS run. In our experiment, we took PSF measurements using a 765nm narrow-band filter. The defocused PSF measurements were made with the camera offset by ±24 mm and ±48 mm about the focus. With a 30mm aperture over the DM surrogate flat, our system has an F/# of about 25.6. Using the relationship

$$d = 8\lambda(F/\#)^2/\Delta z, \tag{1}$$

we can compute that our resulting imagery has ±6 waves and ±12 waves peak-to-valley induced into them.[5]

Although not measured in every run, the pupil image, shown in Figure 3, serves an important constraint in the MGS algorithm. In MGS, it provides both the fundament pupil support constraint as well as the pupil field amplitude constraint.

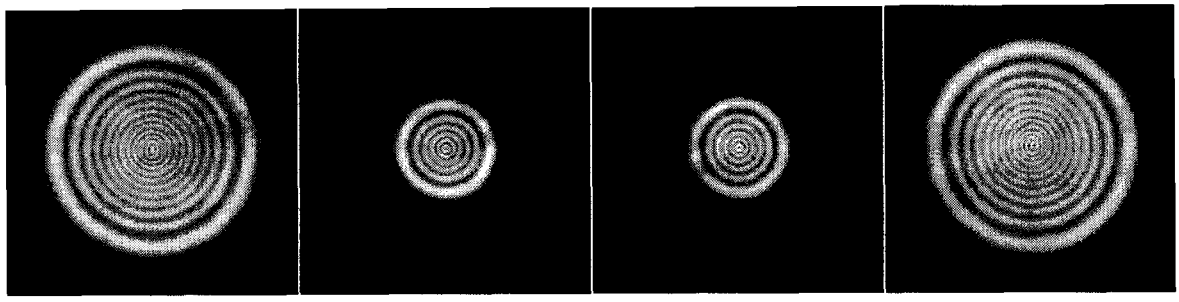

Figure 2: An example of the PSF measurements from one of the WFS runs are shown above (with a square-root intensity scale). The measurements were made using a narrow-band filter with at central wavelength at 765nm and by pistoning the camera through focus by ±48mm (outer pair of defocused PSFs) and ±24mm (inner pair of defocused PSFs). These images combined with a pupil measurement (see Figure 3) make up the complete ensemble data used to estimate the wavefront within a single run.

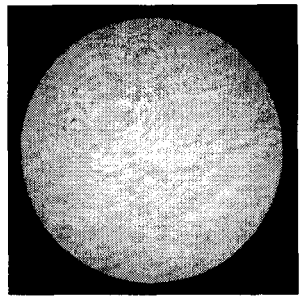

Figure 3: The measurement of system pupil is made by inserting a small lens in front of the camera. Aside from the slow variations in the illumination profile, diffraction effects from dust particles can be seen in this intensity image.

2. EXPERIMENTAL WAVEFRONT SENSING REPEATABILITY

The WFS repeatability experiment consisted of simply taking the sequence of defocused PSF measurements (as shown in Figure 2) repeatedly over a significant time frame. In our experiment, we took 26 separate runs that spanned about 40 hours of continuous time on HCIT. Out of all the runs, 24 of the 26 datasets had complete ensembles of data that consisted of 10 well-exposed PSF measurements per defocus level. The ten exposures provided a total of 2.5×10^9 for ±6 wave defocused pairs of PSF and about 9.3×10^9 photons for the ±12 wave defocused pair. The other two runs where incomplete, having several dropped frames due to software and hardware glitches.

In the analysis of the data, we considered three ways of processing each run with MGS. There is, of course, the *joint processing* of all the defocused PSFs into a single estimated of the optical path difference (OPD) map.[2,3,6] However, we also processed only the *inner pair* (i.e. ±6 wave of defocus) and the *outer pair* (±12 waves of defocus) into separate OPD estimates. This separate processing of the inner and outer pairs, allows us to analyze, to some degree, the optimality of the joint processing and the separate sensitivities that each defocus level has to noise source and model-mismatches.

In Figure 4, we plot the root-mean-square (RMS) of the estimated OPD obtained using MGS from each run along with its variations from the ensemble average for each of the processing methods. These variations are computed in three ways. First, there is the pixel-to-pixel deviation of an individual OPD from the ensemble average. This deviation includes spatial frequencies variations in the estimate that exceed 100 cycles/pupil. Knowing that the anticipated DM will have 30 actuators across the clear-aperture, we also examined the OPD variation within the DM controllable passband of 15 cycles/pupil. It is within this range of frequencies that WFS variations will influence the wavefront control performance on HCIT. Finally, we examine the low-order variation of the WFS by comparing the estimates to the average over the first 15 Zernike modes[7] less piston, tip and tilt.

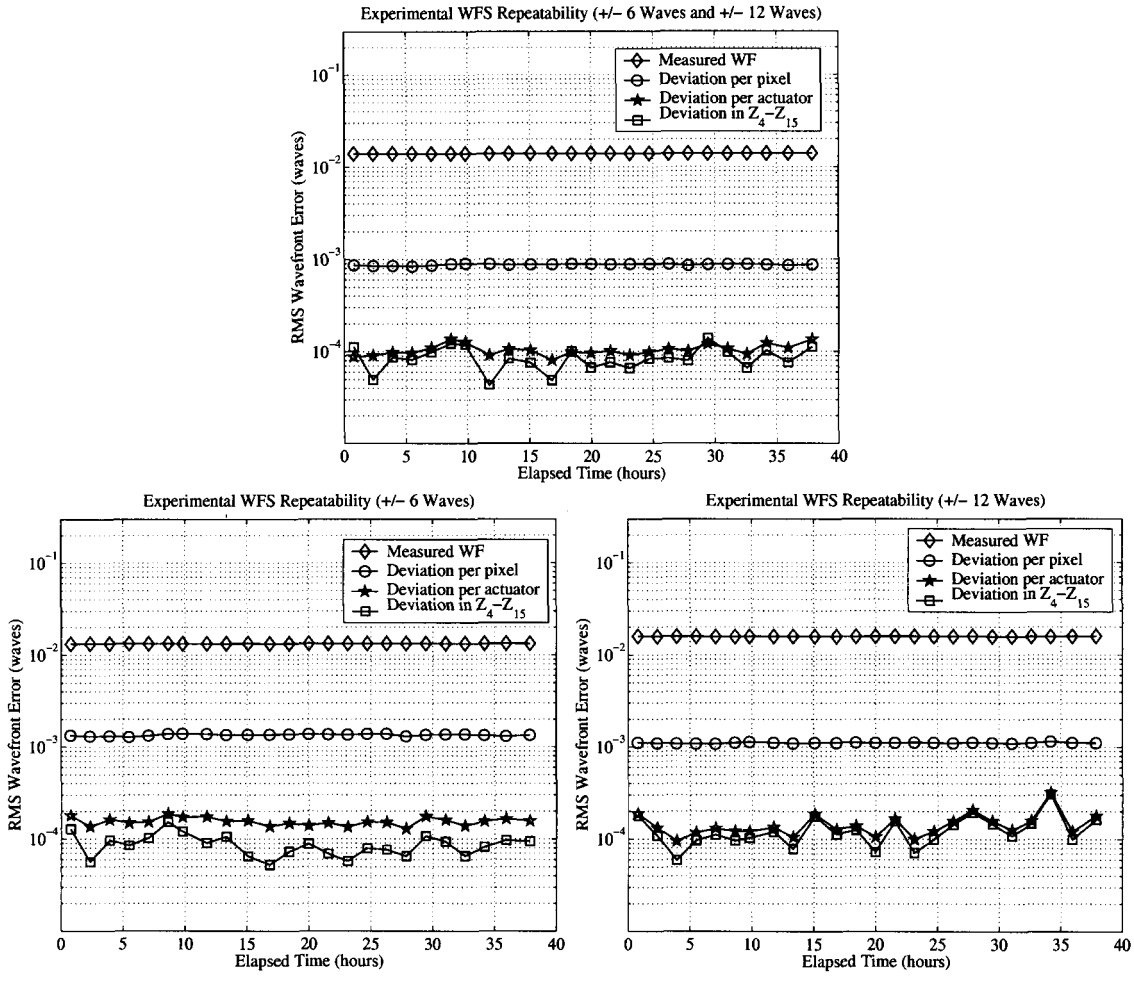

Figure 4: Run by run statistics are shown for the WFS repeatability experiment. The figure on the top row plots the RMS of the OPD estimate from the jointly processed ensemble over the 39 hours that the experiment elapsed. The curves below these points are the deviation from the ensemble averaged OPD that is computed on a per-pixel and per-actuator basis as well as over the low-order Zernike modes. The bottom row shows the results from processing the data using only the inner-pair of defocused PSFs (left) and the outer-pair of defocused PSFs (right). The per-actuator calculations are based on the 15 cycle/pupil controllable passband.

From the plots, we can observe that the WFS repeatability is on the order of $\lambda/1000$ on a pixel-by-pixel basis. However, what really matters is the repeatability within the controllable passband of the DM. Here, the variation is an astounding $\lambda/10{,}000$ - that is about 79 *picometer*s RMS on average. We also observe that a substantial portion of this repeatability error is contained in the low-order modes. With the reduced signal-to-noise ratio (SNR) within their respective data subsets, the inner-pair and outer-pair OPD estimates have slightly increased repeatability error. Interestingly, the WFS repeatability of the low-order modes is considerably poorer for the estimates using only the ± 12 waves of defocus. In Table 1, we summarize the statistical results from our experiment.

Of course, repeatability is not the same accuracy. The average estimates, shown in Figure 5, appears to contain a significant ringing artifact that is inconsistent between the estimates generated by the separate processing of inner and outer defocus pairs; we suspect a static model mismatch error is affecting our estimates at higher levels of defocus. Next

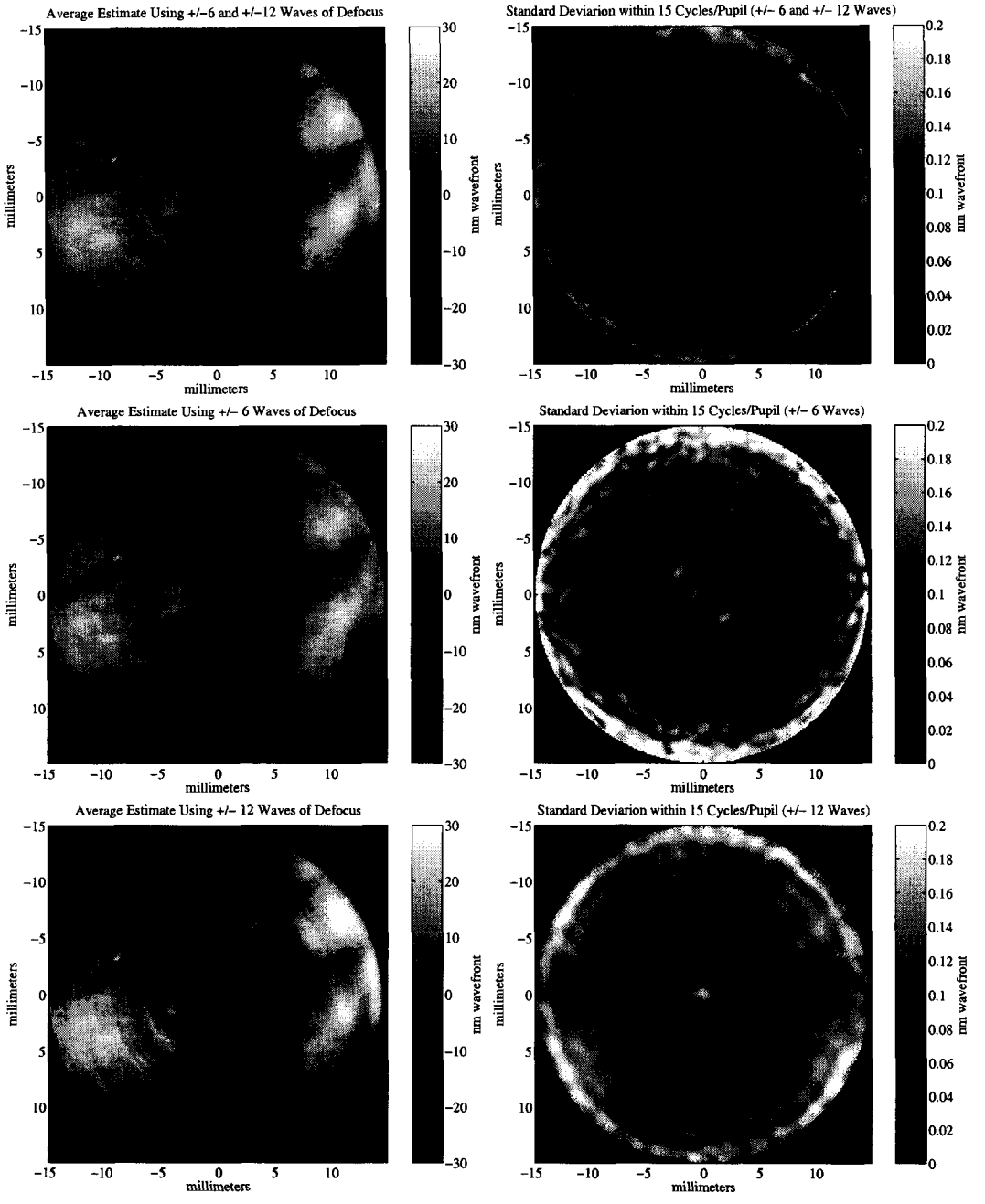

Figure 5: The average and standard deviations through the collections of experiment estimates are shown. The top row has the average OPD estimate (left) and its standard deviation one a per actuator basis (right) for processing jointly the inner and outer pairs of defocus images into estimates. The middle rows show the results of processing only the inner pairs while the bottom row presents the results from processing using only the outer pairs. The images in the right column where created by computing the standard-deviation per pixel through the stack of estimates after the each one has been low-pass filtered to 15 cycle/pupil. This frequency range represents the controllable passband of the planned 32x32 actuator DM.

to these ensemble averages, we show maps of the standard deviation per actuator over the ensemble of estimates. These maps were created by computing the standard deviation per pixel through the stack of estimates after filtering each one down to the controllable passband. The brighter regions in these maps correspond to regions of the OPD that have higher repeatability error. The increased variation near the edge of the maps is consistent with the variations observed with the low-order modes. We can get more insight into these variations, however, by examining the spatial-frequency distribution of the experimental WFS repeatability.

Over the collection of estimates, we compute the power spectral density (PSD) distribution of the OPD as

$$S_{opd}(u,v) = \kappa\left\langle \left| FT\left[opd_n(u,v)\right]\right|^2 \right\rangle_n , \tag{2}$$

where *FT[.]* is a Fourier transforms operation, κ is a normalization constant and n is the index over the WFS runs. The PSD of the variation within the ensemble can be computed likewise as

$$S_{repeat}(u,v) = \kappa\left\langle \left| FT\left[opd_n(u,v) - \left\langle opd_n(u,v)\right\rangle_n\right]\right|^2 \right\rangle_n . \tag{3}$$

Figure 6, show azimuthally averaged plots of the PSD of the OPD estimates and the variation for the three methods of processing. The sets of points about the curves represent the scatter in the PSD about their characteristic. The PSD curves shown for the WFS repeatability error indicate that estimate variations have the strongest energy levels at about 2 cycles/pupil at 10^{-5} waves^2. From 3 to about 40 cycles/pupil this energy runs between 10^{-11} and 10^{-12} waves^2, oscillating in a chirp-like fashion as a function of radial frequency. It can be shown that the contrast floor contribution from a speckle at given energy level E_s is given by $(4\pi)^2 E_s$. This means that the energy in the estimate deviation is consistent with the production of a contrast floor between 10^{-9} and 10^{-10}, provided, of course, that the wavefront is corrected to that level within the frequency band.

Thanks to the recent work of Dean et. al. (see ref. [8]), the chirp-like oscillations that are apparent in the PSD of the estimate deviation can be understood. In their research, it was shown that the modulation of sine-wave aberrations in a defocused PSF intensity goes as $-\sin\left(\pi\nu^2/8d\right)$, where ν is the linear spatial frequency of the aberration and d is the defocus level in waves[8]. In our case, we are experimentally sensing an aberration that spans a large range of spatial frequencies. Assuming that their one-dimensional analysis extends into a two dimensional form with a dependency on radial spatial frequency, ρ (instead of ν), we can compute that the minimum and maximum PSF intensity modulation occurs at

$$\begin{aligned} \rho_{\min} &= \left\{\rho : \rho^2/8d = n\right\} \\ \rho_{\max} &= \left\{\rho : \rho^2/8d = 3n/2\right\} \end{aligned} \qquad n = 0,1,2,.... \tag{4}$$

Looking at the peaks and valleys of the chirp-oscillations in our PSD curves, we find that there is a seemingly perfect correspondence between lower energy in repeatability error and the maxima in the PSF intensity modulation of the aberration at the appropriate spatial frequencies (for the given levels of defocus). Likewise, the peaks of higher energy correspond to the minima of PSF intensity modulation. It appears that the repeatability of MGS WFS is approaching a fundamental limit that is brought fourth by the noise within the collected data.

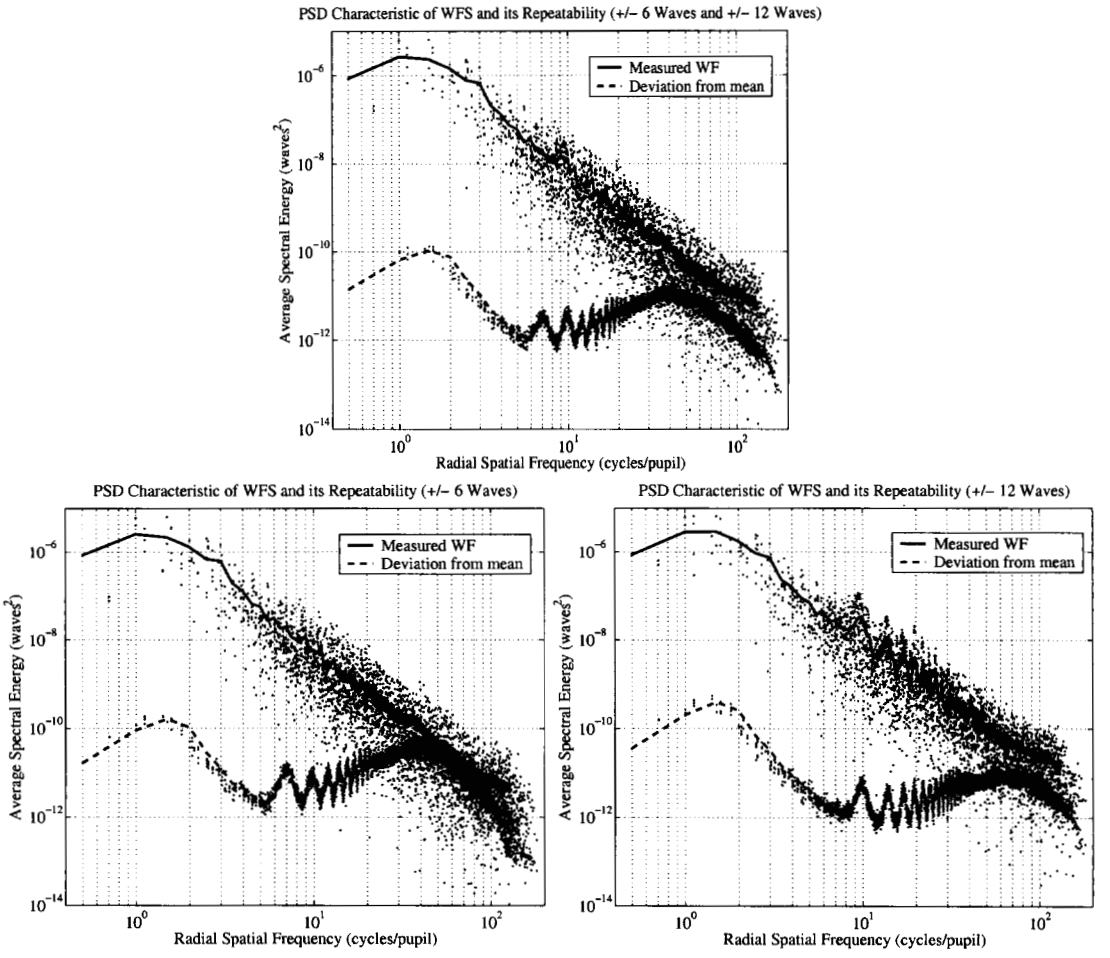

Figure 6: These plots depict the average power-spectral density characteristic for the experiment estimates and their variation over the ensemble. The top-row shows these energy distributions for jointly-processed case as a function of spatial frequency The bottom row shows these results for processing the data using only the inner-pair of defocused PSFs (bottom-left) and for the outer-pair of defocused PSFs (bottom-right).

Table 1: Shown below are the ensemble statistics from the WFS repeatability experiment. All values shown are in waves RMS.

Experimental WFS Repeatability	Defocus Levels Used in Estimation		
Ensemble Statistics (waves rms)	±6 Waves	±12 Waves	±6 Waves, ±12 Waves
Average Estimate	0.01318	0.01576	0.01391
Repeatability Per Pixel	0.00135	0.00112	0.00087
Repeatability Per Actuator	0.00015	0.00015	0.00010
Repeatability in Low-Order Modes	0.00009	0.00013	0.00009

3. ESTIMATING THE STATIC WAVEFRONT SENSING BIAS

While it appears that experimental repeatability of WFS is approaching a fundamental noise limit, there remains evidence that there is a fixed bias error in the estimates. As we pointed out earlier, there is an inconsistency between the inner-pair and outer-pair processed estimates and a version of this difference appears in the jointly processed estimate. Without the ground truth in our experiment, we cannot separate this static error from the repeatability error in the WFS process. Thus, we turn to simulations where we can know the truth.

We set up a repeated sequence of PSF image generation to mimic the repeatability study. The model for creating the simulated PSFs included the appropriate detector sampling, the pupil illumination variations, photon count levels and detector-blur that are consistent with our best knowledge of HCIT. The simulations also included the frame-to-frame variations in the PSF defocus levels and PSF centering that were observed over the actual experiment. For the true OPD in the simulations we used the ensemble mean estimate from the WFS experiment.

We simulated 24 sets of defocused PSF measurements the paralleled the experiment. Using the very same procedures that processed the experimental data (with all its own modeling assumptions and parameters), we created another set of OPD estimates. In terms of repeatability, the simulation is about 1.5 to 2 times better than the experiment. This indicates that there are noises sources (such as read-noise and background light) in the experiment not yet captured in this simulation. It also means that the simulations may serve a lower bound on our estimation of the static bias error. The repeatability statistics for the simulation results are listed in Table 2.

Because we know the true OPD in the simulations, we are now able to study the accuracy of the WFS processes. Table 3 lists the simulation accuracy statistics that were observed. They reveal that while the simulation WFS repeatability reaches $\lambda/15{,}000$, the actual accuracy is a around $\lambda/1500$. Although this static error seems dominated by low-order modes, the error also contains ringing artifacts that are a much weaker version to the ringing that can be observed in the estimates shown in Figure 4.

To best understand the distribution of the accuracy error, we compute the PSD of the error over the collection of OPD estimates by

$$S_{error}(u,v) = \kappa\left\langle \left| FT\left[opd_n(u,v) - opd_{truth}(u,v)\right]\right|^2 \right\rangle_n . \tag{5}$$

In Figure 7, we plot the azimuthally averaged PSD for the OPD truth used in the estimation along with that of the estimation error, and estimation repeatability. The error curves represent the static bias that limits the accuracy of the wavefront estimate as a function of spatial frequency. After removing the portion of the error contained in the low-order terms from the estimates, we can see that the estimation accuracy traces the repeatability curves to within a factor of 10. Like the repeatability curves, it has same chirp oscillations that exhibit a high a degree of correspondence to the PSF intensity modulation formula from [8]. While the contrast of aberration modulation leads to repeatability error in the presence noise, it would appear to also appear to weight in the model mismatches into a static errors in the estimate leading to ringing artifacts in the results.

Unlike the experimental results, the simulations do not have a substantially stronger accuracy errors in its estimates derived from the ±12 wave defocus PSFs. This suggests that there are some unknown fixed modeling errors in WFS algorithm when processing the experimental data.

Table 2: Shown below are the ensemble statistics from the simulation WFS repeatability.

Simulation WFS Repeatability	Defocus Levels Used in Estimation		
Ensemble Statistics (waves rms)	±6 Waves	±12 Waves	±6 Waves, ±12 Waves
Average Estimate	0.01443	0.01367	0.01420
Repeatability Per Pixel	0.00066	0.00058	0.00044
Repeatability Per Actuator	0.00010	0.00009	0.00006
Repeatability in Low-Order Modes	0.00006	0.00008	0.00007

Table 3: Shown below are the ensemble statistics from the simulation WFS accuracy.

Simulation WFS Accuracy	Defocus Levels Used in Estimation		
Ensemble Statistics (waves rms)	±6 Waves	±12 Waves	±6 Waves, ±12 Waves
Accuracy Per Pixel	0.00154	0.00128	0.00116
Accuracy Per Actuator	0.00087	0.00064	0.00068
Accuracy in Low-Order Modes	0.00086	0.00063	0.00068

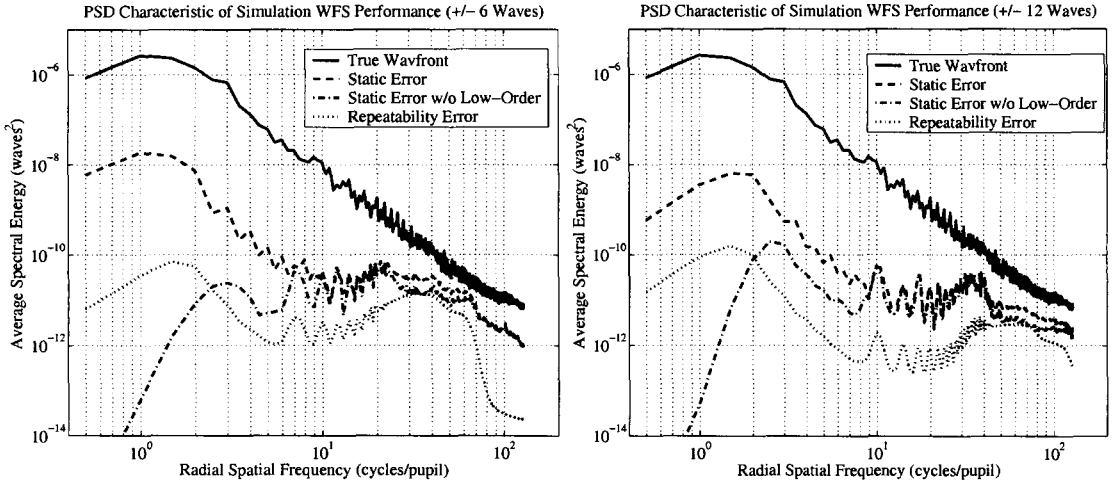

Figure 7: These plots depict the average power-spectral density characteristic for the simulation estimates, their estimation accuracy and their repeatability over the ensemble. Shown are the results for processing the data using solely the inner-pair(left) and outer-pair (right) of defocused PSFs..

4. COMPARISON OF THE EXPERIMENT TO DIFFRACTION MODELING

As a last analysis of our experimental results, we make a comparison of the experiment OPD maps to the results of diffraction modeling. As shown in Figure 1, we have interferometric measurements of all the HCIT optics in their mounted state. We converted these measurements into surface maps and placed them inside a MACOS[§] model of the HCIT. The MACOS model has a complete prescription of the testbed in its original optimized design state. This model is setup to use near-field diffraction to propagate light from optical surface to surface producing a complex field at the camera focal plane. By taking the inverse Fourier transform of this complex field, we obtain a model of the exit-pupil to the camera focal plane.

[§] Modeling and Analysis for Controlled Optical Systems (MACOS) version 2.80.

The original prescription of the testbed is certainly not likely to be in high agreement with actual physical alignment of all the optics. As such, we expect to have differences in the low-order modes and in the portions of the optical surfaces that are actually illuminated by the HCIT light source. In Figure 8 we show the OPD model along with its difference to the average OPD estimates from the experiment (shown in Figure 5). The differences are shown over a 93% clear pupil region. This eliminated the non-common portion of the OPDs caused by a global shear between the model and actual HCIT optics that are illuminated. In these differences, we clearly see the static WFS error we discussed earlier. Along with this static error, there are low-order mode differences combined with fine-scale variations that likely to be from optic-to-optic shearing resulting from the way the beam propagates through the system. The numerical differences summarized in Table 4 show that modeling and experimental results agree to almost the $\lambda/200$ level.

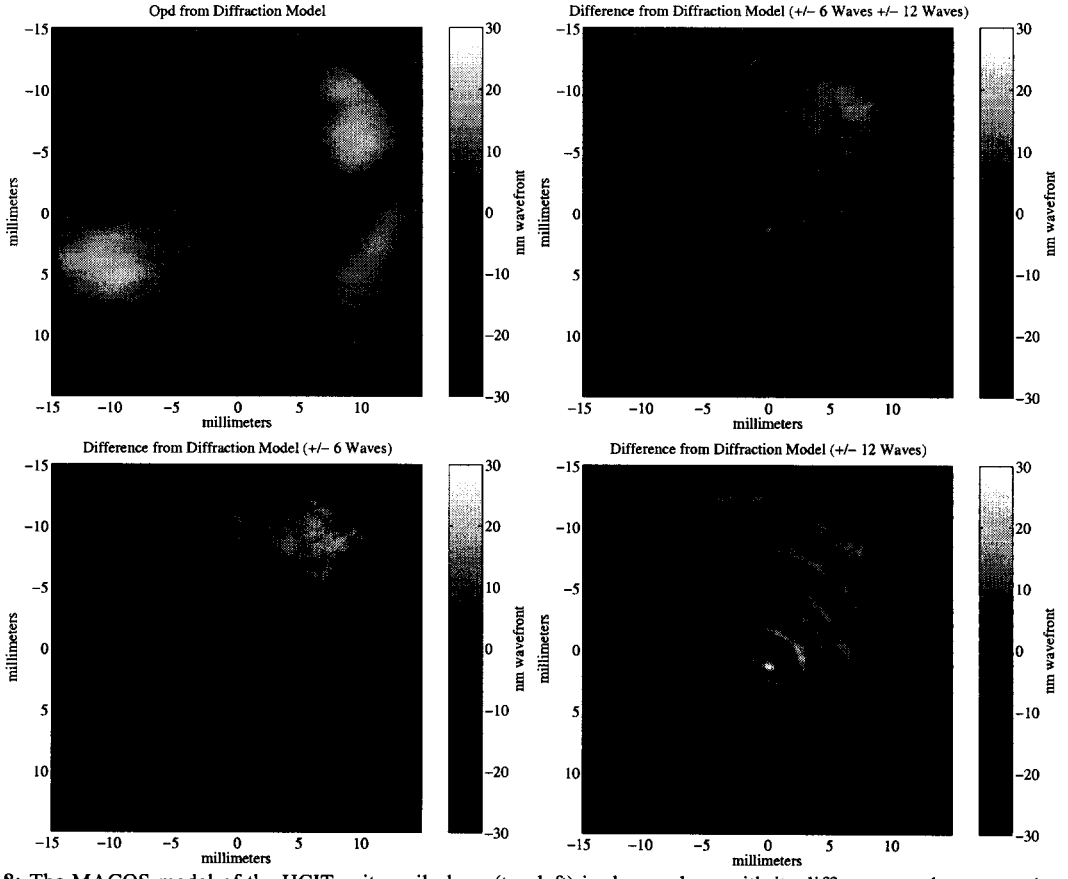

Figure 8: The MACOS model of the HCIT exit-pupil phase (top-left) is shown along with its difference to the averaged estimates from the three methods used to process the experimental data. The differences are shown over the central 93% of the clear aperture.

Table 4: The table below shows the level of consistency between our diffraction model base exit-pupil OPD and the estimated ones from the experiment

Experiment Consistency With Diffraction Model Ensemble Statistics (waves rms)	Defocus Levels Used in Estimation		
	±6 Waves	±12 Waves	±6 Waves, ±12 Waves
Consistency Per Pixel	0.00604	0.00748	0.00605
Consistency Per Actuator	0.00579	0.00698	0.00578
Consistency in Low-Order Modes	0.00540	0.00639	0.00527

5. CLOSING REMARKS

In this paper, we have shown the experimental repeatability of WFS on HCIT is λ/10,000 within the controllable passband of its next DM. Despite the high level of repeatability, simulations that paralleled the experiment would indicate that we have a fixed bias error that is, at the minimum, on the order of λ/1000. The domination of this bias by low-order terms coupled with the ringing artifacts in the estimate indicate that we have some model mismatches in MGS algorithm. The higher levels of ringing artifact ±12 wave data maybe an indication that our assumption that the F/# of this system is fixed is not correct. The fixed F/# assumption is valid only for telecentric systems whose pupil is at infinity. In the near term we will be exploring sensitivity of MGS to mismatches in the F/# of its model to that of the actual optical system. Other avenues to explore include looking at the level of convergence achieve in our model adaptation procedure that precedes the MGS estimation. Failing to converge here will leave behind some residual tilt error that MGS will process into superfluous coma error and ringing atifacts[3].

Regardless of the static bias error, the high level of repeatability demonstrates that HCIT is a very stable testbed and that MGS has the potential to correct the WFE in a coronagraphic telescope from in an initially deployed state to a level that is commensurate with high contrast imaging.

ACKNOWLEDGEMENTS

The research described in this paper was carried out at the Jet Propulsion Laboratory, California Institute of Technology, under a contract with the National Aeronautics and Space Administration.

REFERENCES

1. D. C. Redding, et al, Next Generation Space Telescope wavefront sensing and control, Proc. SPIE, vol. 4850 (Waikoloa 2002).
2. J. J. Green, D. C. Redding, Y. Beregovski, Andrew E. Lowman and Catherine M. Ohara, "Interferometric validation of image based wavefront sensing for NGST,,, Proc. SPIE, vol. 4850 (Waikoloa 2002).
3. J. J. Green, D. C. Redding, S. Shaklan and S. A. Basinger, "Extreme Wave Front Sensing Accuracy for the Eclipse Coronagraphic Space Telescope," Proc. SPIE, vol. 4860 (Waikoloa 2002).
4. J. Trauger, et al, "Eclipse high-contrast imaging test bed,,, Proc. SPIE, vol. 4854 (Waikoloa 2002).
5. D. J. Schroeder, *Astronomical Optics*, Academic Press, San Diego, 2000.
6. S. A. Basinger, D. C. Redding, A. E. Lowman, L. A. Burns, K. Liu and D. Cohen, "Performance of wave front sensing and control algorithms on a segmented telescope testbed,,, Proc. SPIE, *UV, Optical and IR Space Telescopes and Instruments*, vol. 4013, pp. 749-756 (2000).
7. R. J. Noll, "Zernike polynomials and atmospheric turbulence,,, J. Opt. Soc. Am., vol. 66(3), pp. 207-211, 1976.
8. B. H. Dean & C W. Bowers, "Diversity selection for phase-diverse phase retrieval,,, J. Opt. Soc. Am. A., vol 20, pp. 1490-1504, August 2002.
9. John T. Trauger, et al, "Performance of a precision high-density deformable mirror for extremely high contrast imaging astronomy from space,,, Proc. SPIE, vol. 4854 (Waikoloa 2002).
10. F. Malbet, J. W. Yu and M. Shao, "High Dynamic-Range Imaging Using a Deformable Mirror for Space Coronography,,, PASP, vol. 107, pp. 386-398, 1995.
11. J. D. Gaskill, *Linear Systems, Fourier Transforms, and Optics*, John Wiley & Sons, New York, 1978.
12. R. W. Gerchberg and W. O. Saxton, "A Practical Algorithm for the Determination of Phase from Image and Diffraction Plane Pictures,,, *Optik,* vol. 34(2), pp. 237-246. 1972.
13. D. L. Misell, "A method for the solution of the phase problem in electron microscopy,,, J. Phys. D: Appl. Phys., vol. 6, 1973.
14. B. R. Frieden, Probability, Statistical Optics, and Data Testing, Springer-Verlag, Berlin, 1991.